

Controlling spin relaxation with a cavity

A. Bienfait¹, J. J. Pla^{2†}, Y. Kubo^{1†}, X. Zhou^{1,3}, M. Stern^{1,4}, C. C. Lo², C. D. Weis⁵, T. Schenkel⁵, D. Vion¹, D. Esteve¹, J. J. L. Morton² & P. Bertet¹

Spontaneous emission of radiation is one of the fundamental mechanisms by which an excited quantum system returns to equilibrium. For spins, however, spontaneous emission is generally negligible compared to other non-radiative relaxation processes because of the weak coupling between the magnetic dipole and the electromagnetic field. In 1946, Purcell realized¹ that the rate of spontaneous emission can be greatly enhanced by placing the quantum system in a resonant cavity. This effect has since been used extensively to control the lifetime of atoms and semiconducting heterostructures coupled to microwave² or optical^{3,4} cavities, and is essential for the realization of high-efficiency single-photon sources⁵. Here we report the application of this idea to spins in solids. By coupling donor spins in silicon to a superconducting microwave cavity with a high quality factor and a small mode volume, we reach the regime in which spontaneous emission constitutes the dominant mechanism of spin relaxation. The relaxation rate is increased by three orders of magnitude as the spins are tuned to the cavity resonance, demonstrating that energy relaxation can be controlled on demand. Our results provide a general way to initialize spin systems into their ground state and therefore have applications in magnetic resonance and quantum information processing⁶. They also demonstrate that the coupling between the magnetic dipole of a spin and the electromagnetic field can be enhanced up to the point at which quantum fluctuations have a marked effect on the spin dynamics; as such, they represent an important step towards the coherent magnetic coupling of individual spins to microwave photons.

Spin relaxation is the process by which a spin reaches thermal equilibrium by exchanging an energy quantum $\hbar\omega_s$ with its environment (where \hbar is the reduced Planck constant and ω_s is the resonance frequency of the spin), for example in the form of a photon or a phonon, as shown in Fig. 1a. Understanding and controlling spin relaxation is essential in applications such as spintronics⁷, quantum information processing⁸, and magnetic resonance spectroscopy and imaging⁹. For such applications, the spin relaxation time T_1 must be sufficiently long to permit coherent spin manipulation; however, if T_1 is too long, it becomes a major bottleneck that limits the repetition rate of an experiment, which in turn affects factors such as the achievable sensitivity. Certain types of spins can be actively reset to their ground state by optical¹⁰ or electrical¹¹ means, owing to their specific energy-level scheme, and methods such as chemical doping have been used to influence spin relaxation times *ex situ*¹². Nevertheless, an efficient, general and tunable initialization method for spin systems is still currently lacking.

At first inspection, spontaneous emission would appear unlikely to influence spin relaxation: for example, an electron spin in free space and at a typical frequency of $\omega_s/(2\pi) \approx 8$ GHz spontaneously emits photons at a rate of about 10^{-12} s^{-1} . However, the Purcell effect provides a way to markedly enhance spontaneous emission and thus gain precise and

versatile control over spin relaxation¹. Consider a spin embedded in a microwave cavity of quality factor Q and frequency ω_0 . If the cavity damping rate $\kappa = \omega_0/Q$ is greater than the spin–cavity coupling g , then the cavity provides an additional channel for spontaneous emission of microwave photons, governed by the Purcell rate^{6,13}

$$\Gamma_P = \kappa \frac{g^2}{\kappa^2/4 + \delta^2} \quad (1)$$

in which $\delta = \omega_0 - \omega_s$ is the spin–cavity detuning (see Fig. 1a and Methods). This cavity-enhanced spontaneous emission can be much larger than in free space, and is strongest when the spins and cavity are

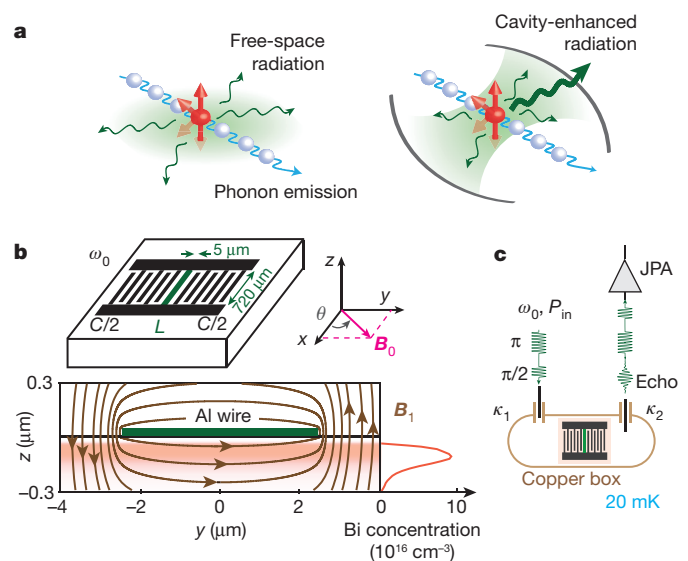


Figure 1 | Purcell-enhanced spin relaxation and experimental set-up. **a**, By placing a spin in a resonant cavity, radiative spin relaxation can be made to dominate over intrinsic processes such as phonon-induced relaxation. **b**, Top, a planar superconducting resonator with frequency $\omega_0 = 1/\sqrt{LC}$ consisting of an interdigitated capacitor (black; with a capacitance C) in parallel with an inductive wire (green; with an inductance L) is fabricated on top of Bi-doped Si. A static magnetic field B_0 is applied parallel to the x – y plane of the 50-nm-thick aluminium layer, with a tunable orientation θ . Bottom, magnetic field lines of the microwave excitation field B_1 generated by the aluminium wire (arrows) are superimposed over the local concentration of Bi donors (red), obtained by secondary ion mass spectrometry (SIMS). **c**, The sample is mounted in a copper box that is thermally anchored at 20 mK, and probed by microwave pulses via asymmetric antennae that are coupled with rate $\kappa_1 \approx \kappa_2/5$ to the resonator. Microwave pulses at ω_0 of power P_{in} are sent by antenna 1, and the microwave signal leaving via antenna 2 is directed to the input of a Josephson parametric amplifier (JPA).

¹Quantronics Group, SPEC, CEA, CNRS, Université Paris-Saclay, CEA-Saclay, 91191 Gif-sur-Yvette, France. ²London Centre for Nanotechnology, University College London, London WC1H 0AH, UK. ³Institute of Electronics Microelectronics and Nanotechnology, CNRS UMR 8520, ISEN Department, Avenue Poincaré, CS 60069, 59652 Villeneuve d'Ascq Cedex, France. ⁴Quantum Nanoelectronics Laboratory, BINA, Bar Ilan University, Ramat Gan, Israel. ⁵Accelerator Technology and Applied Physics Division, Lawrence Berkeley National Laboratory, Berkeley, California 94720, USA. [†]Present addresses: School of Electrical Engineering & Telecommunications, University of New South Wales, Sydney, New South Wales 2052, Australia (J.J.P.); Okinawa Institute of Science and Technology (OIST) Graduate University, Onna, Okinawa 904-0495, Japan (Y.K.).

on resonance ($\delta=0$): $\Gamma_p = 4g^2/\kappa$. Furthermore, the Purcell rate can be modulated by changing the coupling constant or the detuning, allowing spin relaxation to be tuned on demand.

Although the Purcell effect was used to detect spontaneous emission of radiofrequency radiation from nuclear spins coupled to a resonant circuit¹⁴, the corresponding Purcell rate $\Gamma_p \approx 10^{-16} \text{ s}^{-1}$ (or 1 photon emitted every 300 million years) was negligible compared to the intrinsic spin–lattice relaxation processes. For photon emission to become the dominant spin-relaxation mechanism, both a large spin–cavity coupling and a low cavity damping rate are needed; in our experiment, this is achieved by combining the microwave confinement provided by a micrometre-scale resonator with the high quality factors achieved by using superconducting circuits.

The device consists of two planar aluminium lumped-element superconducting resonators (denoted A and B) patterned onto a silicon chip that was purified in nuclear-spin-free ²⁸Si and implanted with bismuth atoms (see Fig. 1b) at a sufficiently low concentration for collective radiation effects to be absent. A static magnetic field B_0 is applied in the plane of the aluminium resonators, at an angle θ from the resonator inductive wire, tunable *in situ*. The device is mounted inside a copper box and cooled to 20 mK. Each resonator can be used to perform inductive detection of the electron-spin resonance (ESR) signal of the bismuth donors: microwave pulses at ω_0 are applied at the resonator input, generating an oscillating magnetic field B_1 around the inductive wire that drives the surrounding spins; the quantum fluctuations of this field, present even when no microwave is applied, are responsible for the Purcell spontaneous emission. Hahn echo pulse sequences¹⁵ are used, resulting in the emission of a spin-echo in the detection waveguide, which is amplified with a sensitivity reaching the quantum limit by a Josephson parametric amplifier¹⁶ before demodulation at room-temperature, yielding the integrated echo signal quadrature A_Q (see Methods). A more detailed description of the set-up is found in ref. 17.

Bismuth is a donor in silicon¹⁸ with a nuclear spin $I=9/2$. At cryogenic temperatures it can bind an electron (with spin $S=1/2$) in addition to those shared with the surrounding Si lattice. The large hyperfine interaction $AS \cdot I$ between the electron and nuclear spin (in which S and I are the electron and nuclear spin operators, and $A/h = 1.475 \text{ GHz}$ with h the Planck constant) produces a splitting of 7.375 GHz between the ground and excited multiplets at zero magnetic field (see Fig. 2a for the complete energy diagram¹⁹). This splitting makes the system ideal for coupling to superconducting circuits^{20,21}. At low fields ($B_0 < 10 \text{ mT}$, compatible with the critical field of aluminium), all $\Delta m_F = \pm 1$ transitions are allowed, where m_F is the projection of the total spin ($F = I + S$) along B_0 . Considering only the transitions with largest matrix element, resonator A ($\omega_{0,A}/(2\pi) = 7.245 \text{ GHz}$, $Q_A = 3.2 \times 10^5$) crosses the $|F, m_F\rangle = |4, -4\rangle \leftrightarrow |5, -5\rangle$ transition, whereas resonator B ($\omega_{0,B}/(2\pi) = 7.305 \text{ GHz}$, $Q_B = 1.1 \times 10^5$) crosses the transitions $|4, -4\rangle \leftrightarrow |5, -5\rangle$, $|4, -3\rangle \leftrightarrow |5, -4\rangle$ and $|4, -2\rangle \leftrightarrow |5, -3\rangle$ (see Fig. 2a, b).

The echo signal A_Q from each resonator as a function of B_0 shows resonances at the expected magnetic fields, split into two peaks each with a full-width at half-maximum of $\Delta\omega/(2\pi) \approx 2 \text{ MHz}$ (see Fig. 2a). As is explained in ref. 17, this splitting is believed to be the result of strain induced in the silicon at the donor implant depth of approximately 100 nm by the aluminium circuit deposited on the surface. In the following, we focus on the lower-frequency peak of the $|4, -4\rangle \leftrightarrow |5, -5\rangle$ line, which corresponds to spins lying under the wire. Over the region occupied by these spins, the amplitude of the B_1 field varies by less than $\pm 2\%$, as evidenced by the well-defined Rabi oscillations observed when we sweep the power of the refocusing pulse P_{in} at the cavity input (see Fig. 2c), which allows us to determine the input power of a π pulse for a given pulse duration.

We measure the relaxation time T_1 by performing an “inversion-recovery” experiment²² (see schematic in Fig. 2d), with the static field B_0 aligned along x ($\theta = 0$). A π pulse first inverts the spins whose frequencies lie within the resonator bandwidth $\kappa_{A,B}/(2\pi) = 23 \text{ kHz}$ or

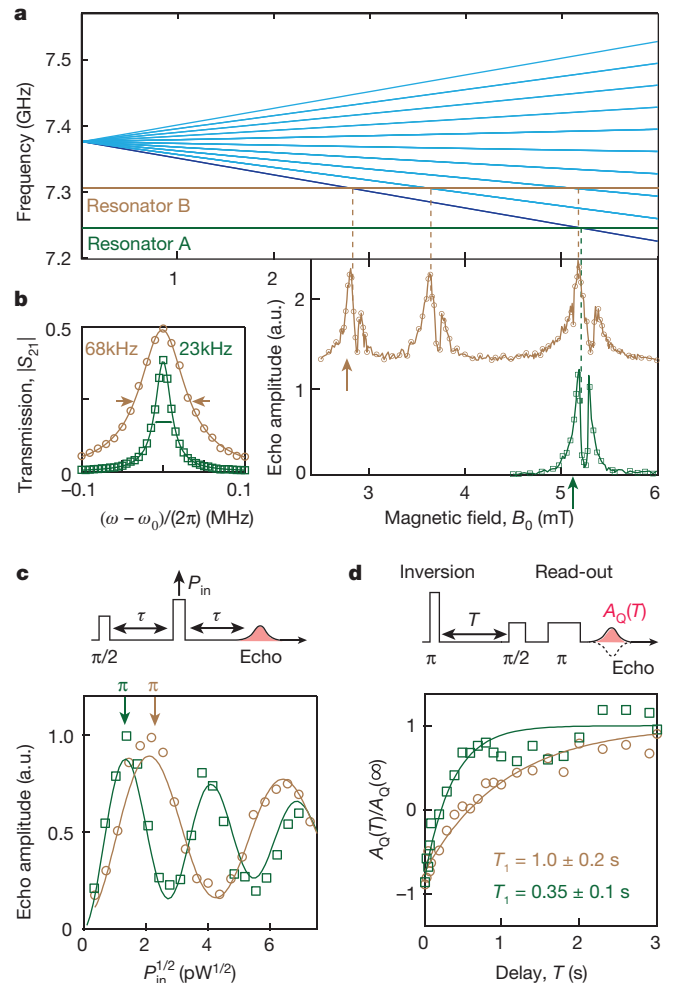


Figure 2 | ESR spectroscopy and Purcell-limited T_1 measurement.

a, Top, dominant electron spin resonance transitions of the Si:²⁰⁹Bi spin system (see Methods). We use two resonators, A (green) and B (brown), with frequencies of 7.246 GHz and 7.305 GHz, respectively, that cross up to three spin transitions in the magnetic field range 0–6 mT, as seen in the echo-detected magnetic field sweep (bottom; vertically offset for clarity). Subsequent spin relaxation measurements were made at the magnetic fields indicated by the arrows, corresponding to the $|F, m_F\rangle = |4, -4\rangle \leftrightarrow |5, -5\rangle$ transition for each resonator. The doublet structure of each transition is caused by strain exerted by the aluminium film on the donors¹⁷. **b**, Cavity linewidths for resonators A and B are found to be 23 kHz and 68 kHz, respectively, from fits (solid lines) to their measured transmission amplitude. **c**, Rabi oscillations are driven by varying the cavity input power of the refocusing π pulse (5 μs long) applied $\tau = 300 \mu\text{s}$ after the first $\pi/2$ pulse. Solid lines are exponentially damped sinusoidal fits. **d**, The inversion-recovery sequence is used to measure the spin relaxation time T_1 . Spin polarization is measured with a Hahn echo sequence. A_Q is rescaled by its value for $T \gg T_1$ ($A_Q(\infty)$) such that it varies from -1 when the spins are fully inverted to $+1$ at thermal equilibrium (see Methods for full sequence description). Data were obtained with the static field B_0 parallel to the inductor ($\theta = 0$). Solid lines are exponential fits to the data with time constant T_1 . The uncertainty is provided by the standard deviation in the exponential fit parameters. a.u., arbitrary units. In all panels, the symbols represent data for each resonator (A, green squares; B, brown circles).

$\kappa_B/(2\pi) = 68 \text{ kHz}$; this constitutes a small subset of the total number of spins because $\kappa_{A,B} \ll \Delta\omega$. After a varying delay T , a Hahn echo sequence provides a measure of the longitudinal spin polarization. By fitting the data with decaying exponentials, we extract $T_1 = 0.35 \text{ s}$ for resonator A and $T_1 = 1.0 \text{ s}$ for resonator B.

To quantitatively compare our results with the expected Purcell rate, it is necessary to evaluate the spin–resonator coupling constant

$g = \gamma_e \langle F, m_F | S_x | F+1, m_F-1 \rangle \| \delta \mathbf{B}_\perp \|$, in which $\gamma_e / (2\pi) \approx 28 \text{ GHz T}^{-1}$ is the electronic gyromagnetic ratio, S_x is the dimensionless Pauli operator for the electron spin and $\delta \mathbf{B}_\perp$ is the component of the resonator-field vacuum fluctuations orthogonal to \mathbf{B}_0 (see Methods). A numerical estimate yields $g_0 / (2\pi) = 56 \pm 1 \text{ Hz}$ for the spins located below the inductive wire in the resonator that are probed in our measurements, and for $\theta = 0$. An independent estimate is obtained by measuring Rabi oscillations: their frequency $\Omega_R = 2g_0 \sqrt{\bar{n}}$ directly yields g_0 given knowledge of the average intra-cavity photon number \bar{n} , which can be determined with about 30% imprecision from P_{in} and the measured resonator coupling to the input and output antennae (see Methods). Using this method, we obtain $g_0 / (2\pi) = 50 \pm 7 \text{ Hz}$ for resonator A and $58 \pm 7 \text{ Hz}$ for resonator B, compatible with the numerical estimate. The corresponding Purcell time of the resonant spontaneous emission is $\Gamma_p^{-1} = 0.36 \pm 0.09 \text{ s}$ for resonator A and $\Gamma_p^{-1} = 0.81 \pm 0.17 \text{ s}$ for resonator B, in agreement with the experimental values.

According to equation (1), a Purcell-limited T_1 should be strongly dependent on the spin-cavity detuning. We introduce a pulse in the magnetic field of duration T between the spin excitation and the spin-echo sequence (see Fig. 3a), which results in a temporary detuning δ of the spins. The amplitude of the echo signal A_Q as a function of T yields their energy relaxation time while they are detuned by δ . To minimize the influence of spin diffusion²², the spin excitation is performed by a high-power long-duration saturating pulse (see Fig. 3a and Methods) instead of an inversion pulse as in Fig. 2d. As is evident in Fig. 3b, we find that the decay of the echo signal is well fitted by a single exponential with a decay time that increases with $|\delta|$. The extracted $T_1(\delta)$ curve (see Fig. 3c) shows an increase in T_1 of up to three orders of magnitude when the spins are detuned away from resonance, until it becomes limited by a non-radiative energy decay mechanism with characteristic time $\Gamma_{\text{NR}}^{-1} = 1,600 \pm 300 \text{ s}$. Given the doping concentration in our sample, this non-radiative decay time is consistent with earlier measurements of donor spin relaxation times²³, which have been attributed to charge hopping, but it could also arise here from spatial diffusion of the spin magnetization away from the resonator mode volume. It is shown in Fig. 3c that the $T_1(\delta)$ measurements are in agreement with the expected dependence $(\Gamma_p(\delta) + \Gamma_{\text{NR}})^{-1}$, with Γ_{NR} the only free parameter in this fit.

Having demonstrated the effect of cavity linewidth and detuning on the Purcell rate, we explore the effect of modulating the spin-cavity coupling constant g . This can be achieved by varying the orientation θ of the static magnetic field \mathbf{B}_0 in the x - y plane (Fig. 1b), which adjusts the component of the microwave magnetic field (\mathbf{B}_1 , which is mostly aligned along y under the inductive wire) that is orthogonal to \mathbf{B}_0 . More precisely

$$g(\theta) = \gamma_e \langle F, m_F | S_x | F+1, m_F-1 \rangle \sqrt{\delta B_{1,y}^2 \cos^2(\theta) + \delta B_{1,z}^2} \quad (2)$$

(since $\delta B_{1,x} = 0$). This orientation dependence is verified experimentally by measuring the Rabi frequency as a function of θ , as shown in Fig. 4a, b, which allows us to extract $g(0) / (2\pi) = 58 \text{ Hz}$ and $g(\pi/2) / (2\pi) = 17 \text{ Hz}$. As expected, we measure longer spin relaxation times for increasing values of θ , as shown in Fig. 4c, with the relaxation rate T_1^{-1} scaling as $[g(\theta)]^2$, in agreement with equation (1). Overall, the data in Figs 3 and 4 demonstrate unambiguously that cavity-enhanced spontaneous emission is by far the dominant spin-relaxation channel when the spins are resonant with the cavity, because the probability of a spin-flip occurring as a result of emission of a microwave photon in the cavity is $1 / [1 + \Gamma_{\text{NR}} / \Gamma_p(\delta=0)] = 0.999$, very close to unity.

The spontaneous emission evidenced here is an energy-relaxation mechanism that does not require the presence of a macroscopic magnetization to be effective. Under the Purcell effect, each spin independently relaxes towards thermal equilibrium by microwave photon emission, so that when no intra-cavity thermal field is present, the sample ends up in a fully polarized state after a time longer than Γ_p^{-1} , regardless of its initial state. This is in stark contrast to the well-known

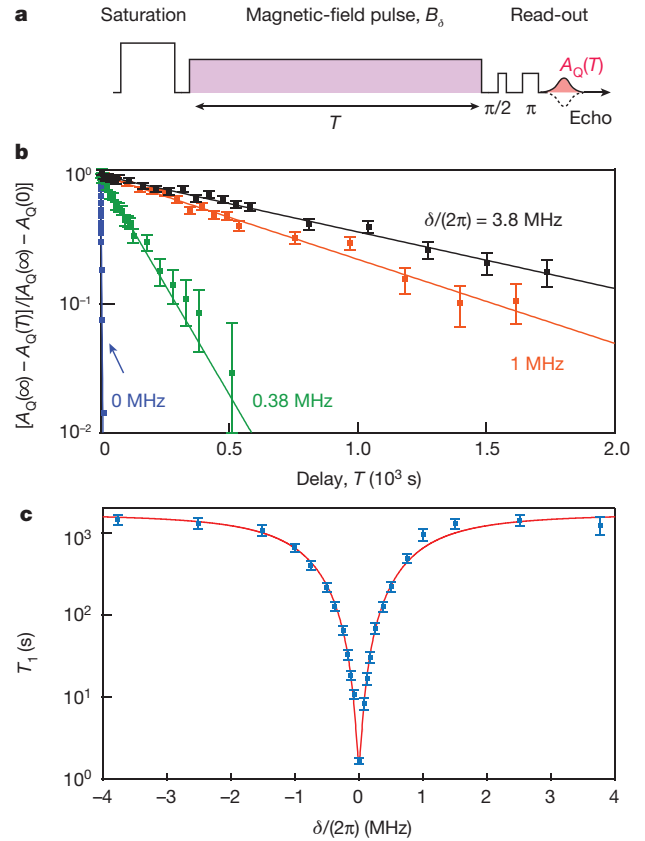


Figure 3 | Controlling Purcell relaxation by spin-cavity detuning.

a, In between their saturation and subsequent read-out, the spins are detuned from the cavity by $\delta = \frac{d\omega_s}{dB} B_\delta$ by applying a magnetic-field pulse with an amplitude of B_δ , with $\frac{1}{2\pi} \frac{d\omega_s}{dB} \approx 25 \text{ GHz T}^{-1}$ for this transition and magnetic field. **b**, Measured spin-polarization decays (symbols) for four different detunings δ , which are well fitted by exponential decays (lines), with relaxation time constants T_1 increasing with the detuning (error bars indicate the standard deviation of a measured echo). **c**, Measured T_1 as a function of detuning δ (blue symbols). The red line is a fit with $(\Gamma_p(\delta) + \Gamma_{\text{NR}})^{-1}$, yielding $\Gamma_{\text{NR}}^{-1} = 1,600 \text{ s}$. Error bars are estimates of the standard deviation of the fit. These measurements are taken using resonator B and with $\theta = \pi/4$, which results in $T_1 = 1.7 \text{ s}$ at $\delta = 0$.

phenomenon of radiative damping²⁴ of a transverse magnetization generated by earlier microwave pulses, which is a coherent collective effect under which the degree of polarization of a sample cannot increase. Had our device possessed a larger spin concentration, spontaneous relaxation would have occurred collectively, manifesting itself as a non-exponential decay of the echo signal on a timescale faster than Γ_p^{-1} (ref. 13), and leading to an incomplete thermalization^{6,25}. The existence of such super-radiant or maser emission²⁶ requires the dimensionless ‘co-operativity’ parameter $C = N g^2 / (\kappa \Delta \omega)$ (where N is the total number of spins) to satisfy $C \gg 1$ (refs 6, 25, 27), which is not the case here because of the large inhomogeneous broadening of the spin resonance caused by strain.

Our demonstrated ability to modulate spin relaxation through three orders of magnitude by changing the applied field by less than 0.1 mT opens up new perspectives for spin-based quantum information processing: long intrinsic relaxation times, which are desirable to maximize the spin coherence time, can be combined with fast, on-demand initialization of the spin state. Similarly, performing electron spin resonance at dilution refrigerator temperatures can be prohibitively slow without the ability to accelerate spin relaxation on demand. We also anticipate that Purcell relaxation will offer a powerful approach to dynamical nuclear polarization^{28,29}, for example, by tuning the cavity to match an electron-nuclear spin flip-flop transition, enhancing the rate of

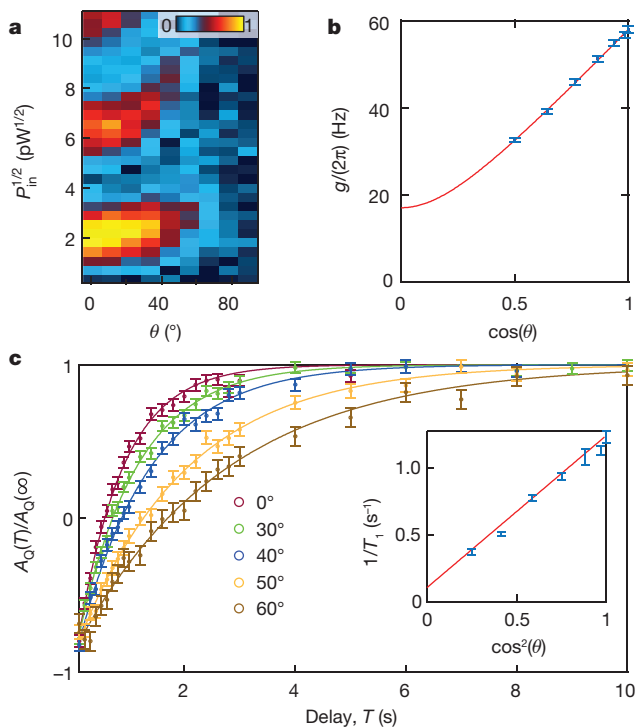


Figure 4 | Dependence of Purcell relaxation on spin-cavity coupling g . **a**, Rabi oscillations (as in Fig. 2c) measured as a function of field orientation θ (see Fig. 1b); the colour scale indicates the echo amplitude in arbitrary units. **b**, The Rabi oscillations in **a** are used to extract the spin-cavity coupling strength g (blue symbols; error bars are determined by the 30% accuracy on P_{in}). These data are fit to equation (2) (red line); the non-zero value of $g(\pi/2)$ is due to the finite out-of-plane component of the microwave magnetic field. **c**, Inversion-recovery measurements (error bars indicate the standard deviation of a measured echo) for different values of θ confirm that the relaxation time T_1 (see inset; error bars are estimates of the standard deviation of the fit) varies as $[g(\theta)]^2$. The red line in the inset is the Purcell formula predicted using the $g(\theta)$ dependence fitted from **b**. All data were collected using resonator B.

cross-relaxation to pump polarization into the desired nuclear spin state³⁰ (see Methods). The Purcell rate we obtain could be increased by reducing the transverse dimensions of the inductor wire to yield larger coupling constants (up to 5–10 kHz), which would reduce the spontaneous emission time to less than 1 ms (thus permitting faster repetition rates and a higher sensitivity¹⁷), allowing for the possibility of high-co-operativity coupling of a single spin to the microwave cavity field. Our measurements constitute evidence that vacuum fluctuations of the microwave field can affect the dynamics of spins, and, therefore, are a step towards the application of concepts in circuit quantum electrodynamics to individual spins in solids.

Online Content Methods, along with any additional Extended Data display items and Source Data, are available in the online version of the paper; references unique to these sections appear only in the online paper.

Received 24 August; accepted 11 December 2015.

Published online 15 February 2016.

- Purcell, E. M. Spontaneous emission probabilities at radio frequencies. *Phys. Rev.* **69**, 681 (1946).
- Goy, P., Raimond, J. M., Gross, M. & Haroche, S. Observation of cavity-enhanced single-atom spontaneous emission. *Phys. Rev. Lett.* **50**, 1903–1906 (1983).
- Heinzen, D. J., Childs, J. J., Thomas, J. E. & Feld, M. S. Enhanced and inhibited visible spontaneous emission by atoms in a confocal resonator. *Phys. Rev. Lett.* **58**, 1320–1323 (1987).

- Yamamoto, Y., Machida, S., Horikoshi, Y., Igeta, K. & Bjork, G. Enhanced and inhibited spontaneous emission of free excitons in GaAs quantum wells in a microcavity. *Opt. Commun.* **80**, 337–342 (1991).
- Gérard, J. M. *et al.* Enhanced spontaneous emission by quantum boxes in a monolithic optical microcavity. *Phys. Rev. Lett.* **81**, 1110–1113 (1998).
- Butler, M. C. & Weitekamp, D. P. Polarization of nuclear spins by a cold nanoscale resonator. *Phys. Rev. A* **84**, 063407 (2011).
- Sinova, J. & Žutić, I. New moves of the spintronics tango. *Nature Mater.* **11**, 368–371 (2012).
- Ladd, T. D. *et al.* Quantum computers. *Nature* **464**, 45–53 (2010).
- Levitt, M. H. *Spin Dynamics: Basics of Nuclear Magnetic Resonance* (John Wiley & Sons, 2001).
- Robledo, L. *et al.* High-fidelity projective read-out of a solid-state spin quantum register. *Nature* **477**, 574–578 (2011).
- Pla, J. J. *et al.* A single-atom electron spin qubit in silicon. *Nature* **489**, 541–545 (2012).
- Shapiro, M. G. *et al.* Directed evolution of a magnetic resonance imaging contrast agent for noninvasive imaging of dopamine. *Nature Biotechnol.* **28**, 264–270 (2010).
- Wood, C. J., Borneman, T. W. & Cory, D. G. Cavity cooling of an ensemble spin system. *Phys. Rev. Lett.* **112**, 050501 (2014).
- Sleator, T., Hahn, E. L., Hilbert, C. & Clarke, J. Nuclear-spin noise. *Phys. Rev. Lett.* **55**, 1742–1745 (1985).
- Hahn, E. Spin echoes. *Phys. Rev.* **80**, 580–594 (1950).
- Zhou, X. *et al.* High-gain weakly nonlinear flux-modulated Josephson parametric amplifier using a SQUID array. *Phys. Rev. B* **89**, 214517 (2014).
- Bienfait, A. *et al.* Reaching the quantum limit of sensitivity in electron spin resonance. *Nature Nanotechnol.* <http://dx.doi.org/10.1038/nnano.2015.282> (2015).
- Feher, G. Electron spin resonance experiments on donors in silicon. I. Electronic structure of donors by the electron nuclear double resonance technique. *Phys. Rev.* **114**, 1219–1244 (1959).
- Wolfowicz, G. *et al.* Decoherence mechanisms of ²⁰⁹Bi donor electron spins in isotopically pure ²⁸Si. *Phys. Rev. B* **86**, 245301 (2012).
- Morley, G. W. *et al.* The initialization and manipulation of quantum information stored in silicon by bismuth dopants. *Nature Mater.* **9**, 725–729 (2010).
- George, R. E. *et al.* Electron spin coherence and electron nuclear double resonance of Bi donors in natural Si. *Phys. Rev. Lett.* **105**, 067601 (2010).
- Schweiger, A. & Jeschke, G. *Principles of Pulse Electron Paramagnetic Resonance* (Oxford Univ. Press, 2001).
- Feher, G. & Gere, E. A. Electron spin resonance experiments on donors in silicon. II. Electron spin relaxation effects. *Phys. Rev.* **114**, 1245–1256 (1959).
- Bloembergen, N. & Pound, R. V. Radiation damping in magnetic resonance experiments. *Phys. Rev.* **95**, 8–12 (1954).
- Wood, C. J. & Cory, D. G. Cavity cooling to the ground state of an ensemble quantum system. Preprint at <http://arXiv.org/abs/1506.03007> (2015).
- Feher, G., Gordon, J. P., Buehler, E., Gere, E. A. & Thurmond, C. D. Spontaneous emission of radiation from an electron spin system. *Phys. Rev.* **109**, 221–222 (1958).
- Temnov, V. V. & Woggon, U. Superradiance and subradiance in an inhomogeneously broadened ensemble of two-level systems coupled to a low-Q cavity. *Phys. Rev. Lett.* **95**, 243602 (2005).
- Carver, T. R. & Slichter, C. P. Polarization of nuclear spins in metals. *Phys. Rev.* **92**, 212–213 (1953).
- Abraham, A. & Goldman, M. Principles of dynamic nuclear polarisation. *Rep. Prog. Phys.* **41**, 395–467 (1978).
- Bloembergen, N., Shapiro, S., Pershan, P. S. & Artman, J. O. Cross-relaxation in spin systems. *Phys. Rev.* **114**, 445–459 (1959).

Acknowledgements We acknowledge technical support from P. Sénat, D. Duet, J.-C. Tack, P. Pari and P. Forget, as well as discussions within the Qnantronics group. We acknowledge support of the European Research Council under the European Community's Seventh Framework Programme (FP7/2007-2013) through grant agreements No. 615767 (CIRQUSS), 279781 (ASCENT) and 630070 (quRAM), and of the C'Nano IdF project QUANTROCRYO. J.J.L.M. is supported by the Royal Society. C.C.L. is supported by the Royal Commission for the Exhibition of 1851. T.S. and C.D.W. were supported by the US Department of Energy under contract DE-AC02-05CH11231.

Author Contributions A.B., J.J.P., J.J.L.M. and P.B. designed the experiment. X.Z. and D.V. designed and fabricated the Josephson Parametric Amplifier. C.C.L., C.D.W. and T.S. provided the bismuth-implanted isotopically purified silicon sample. A.B., J.J.P. and Y.K. fabricated the sample and performed the measurements. A.B., J.J.P., Y.K., J.J.L.M. and P.B. analysed the data. J.J.L.M., D.E., D.V. and P.B. supervised the project. A.B., J.J.P., Y.K., M.S., D.V., D.E., J.J.L.M. and P.B. contributed to writing the paper.

Author Information Reprints and permissions information is available at www.nature.com/reprints. The authors declare no competing financial interests. Readers are welcome to comment on the online version of the paper. Correspondence and requests for materials should be addressed to P.B. (patrice.bertet@cea.fr).

METHODS

Bismuth donors in silicon. Bismuth donors in silicon have the following isotropic spin Hamiltonian³¹: $\hat{H}/\hbar = \mathbf{B} \cdot (\gamma_e \mathbf{S} \otimes \mathbf{1} - \gamma_n \mathbf{1} \otimes \mathbf{I}) + \mathbf{A} \mathbf{S} \cdot \mathbf{I}$, in which the electronic gyromagnetic ratio $\gamma_e/(2\pi) = 27.997 \text{ GHz T}^{-1}$, the nuclear gyromagnetic ratio $\gamma_n/(2\pi) = 6.9 \text{ MHz T}^{-1}$ and the hyperfine coupling constant $A/\hbar = 1.475 \text{ GHz}$. For a weak static field \mathbf{B}_0 ($B_0 \lesssim 50 \text{ mT}$) oriented along x , the eigenstates of the total angular momentum $F = S + I$ and its projection m_F along \mathbf{B}_0 represent good quantum numbers for the 20 electro-nuclear energy states of the Bi:Si system. These eigenstates can be grouped in an $F = 4$ ground and an $F = 5$ excited multiplet separated by a frequency of $(I + 1/2)A/\hbar = 7.35 \text{ GHz}$ in zero-field (see Fig. 1d). Transitions between states that verify $\Delta F \Delta m_F = \pm 1$ can be excited with a field oriented along y (or z) because their associated matrix element $\langle F, m_F | S_y | F + 1, m_F \pm 1 \rangle = \langle F, m_F | S_z | F + 1, m_F \pm 1 \rangle$ has the same magnitude as an ideal electronic spin 1/2 transition $\langle m_s | S_y | m_s \rangle = 0.5$. Only the ten transitions with a matrix element greater than 0.25 are shown in Fig. 2a. Characteristics for the transitions probed by our resonators are given in Extended Data Table 1.

Single-spin coupling to the resonator. The spin-resonator interaction is described by a Jaynes-Cummings Hamiltonian, $\hbar g(a^\dagger \sigma_- + a \sigma_+)$, in which a (a^\dagger) is the field annihilation (creation) operator, σ_- (σ_+) is the spin lowering (raising) operator and g is the spin-resonator coupling strength. For the Bi:Si transitions, $|F, m_F\rangle \leftrightarrow |F + 1, m_F - 1\rangle$ probed by the resonators, g can be expressed as $g = \gamma_e \langle F, m_F | S_x | F + 1, m_F - 1 \rangle \|\delta \mathbf{B}_\perp\|$ (ref. 17), in which $\delta \mathbf{B}_\perp$ is the component of the resonator-field vacuum fluctuations orthogonal to \mathbf{B}_0 . Considering the orientations for \mathbf{B}_0 and $\delta \mathbf{B}$ shown in Fig. 1b, we obtain equation (2)

$$g(\theta) = \gamma_e \langle F, m_F | S_x | F + 1, m_F - 1 \rangle \sqrt{\delta B_{1,y}^2 \cos^2(\theta) + \delta B_{1,z}^2}$$

To estimate the distribution of the coupling constant $g(0)$ for a given transition, we need to estimate the vacuum-field fluctuations $\delta \mathbf{B}_1$ in the spin ensemble region. This is achieved using the COMSOL software and assuming a non-homogeneous current-density distribution in the superconducting aluminium wire³². The total current flowing through the wire cross-section is $\delta i = \omega_0 \sqrt{\hbar/2Z_0}$, in which $Z_0 = \sqrt{L/C}$ is the resonator impedance, determined to be 44Ω via electromagnetic simulations realized in CST Microwave Studio. In all the work presented in the main text, the measurements were done on the low-field peak of transition $|F, m_F\rangle = |4, -4\rangle \leftrightarrow |5, -5\rangle$, which has been attributed to spins residing under the wire. From the spin implantation profile (see Fig. 1b) and the spatial dependence of the microwave field $\delta \mathbf{B}_1$ restrained to the area under the wire ($|y| < 2.5 \mu\text{m}$), the relevant coupling-constant distribution can be extracted. Doing so yields a very asymmetric coupling distribution that is sharply peaked around $g/(2\pi) = 56 \text{ Hz}$ with a 2-Hz full-width at half-maximum for the transition $|4, -4\rangle \leftrightarrow |5, -5\rangle$ with $\theta = 0$. A more detailed derivation of the coupling constant and its estimate at $\theta = 0^\circ$ is available in ref. 17.

Average intra-cavity photon number \bar{n} . The average intra-cavity photon number \bar{n} of a pulse of power P_{in} at the cavity input is evaluated as $\bar{n} = \frac{4\kappa_1 P_{\text{in}}}{\hbar\omega_0(\kappa_1 + \kappa_2 + \kappa_L)^2}$,

in which κ_1 and κ_2 are the couplings to the input and output antennas and κ_L represents the internal losses of the resonator. From a previous calibration of the experimental setup¹⁷, we estimate that we can determine P_{in} with an accuracy of approximately 1 dB. The values of κ_1 , κ_2 and κ_L are determined experimentally by measuring each element of the resonator scattering matrix and fitting to the well-known input-output formulae³³; see Extended Data Table 2.

Data acquisition and echo signal. The full description of the experimental set-up is available in ref. 17. The use of a Josephson parametric amplifier allows us to reach a quantum-limited sensitivity. In addition to the Hahn echo sequence, we use a Carr-Purcell-Meiboom-Gill sequence³⁴ for every echo acquisition. For all A_Q data points presented in this work, 10 π pulses are added after the first echo to recover 10 extra echoes, which are subsequently averaged to boost the signal-to-noise ratio. This scheme allows us to acquire data in single-shot read-out. Each A_Q data point is a single-shot measurement and the error bars are determined by the variance of a pool of at least $n = 200$ measurements, taken in similar conditions.

Experimental determination of T_1 at resonance. The inversion-recovery sequence is used to measure the spin relaxation time T_1 ; see Fig. 2d. Spin polarization is measured with the following Hahn echo sequence: 50- μs -long $\pi/2$ pulse, delay $\tau = 500 \mu\text{s}$, and 100- μs -long π pulse. The pulse durations were chosen such that only spins within a narrow spectral range were detected, producing a well-defined Purcell-limited T_1 . Indeed, because the probed ensemble of spins has a larger linewidth $\Delta\omega = 2 \text{ MHz}$ than do our resonators, the signal emitted during the spin-echo comes from a subset of the ensemble of spins, with a frequency spectrum at least as large as the resonator bandwidth. Spins probed at the edges of the bandwidth of the resonator will have longer Purcell relaxation times; for instance, those detuned by $\delta = \kappa$ have an expected Purcell relaxation time that

is five times slower than the T_1 time expected at perfect resonance; see Extended Data Fig. 1a. The contribution of those spins with a longer decay time to the signal will result in an averaging effect, meaning that the measured T_1 will be erroneously longer than predicted.

To suppress this effect, we reduce the bandwidth of the read-out sequence to collect signal only from spins very close to the resonance. The response function of a pulse of length t_p incident on a cavity with bandwidth κ at frequency ω_0 is expressed as

$$\mathcal{R}(\omega) = [2\text{sinc}(t_p(\omega - \omega_0)/2)]^2 \mathcal{R}_{\text{cav}}(\omega) = \frac{[2\text{sinc}(t_p(\omega - \omega_0)/2)]^2}{1 + 4(\omega - \omega_0)^2/\kappa^2}$$

in which $\text{sinc}(x) = \sin(x)/x$. As shown in Extended Data Fig. 1a, for the narrowest bandwidth $\kappa/(2\pi) = 23 \text{ kHz}$ of resonator A, pulses of 5 μs are heavily filtered by the resonator and have the same bandwidth, whereas 100- μs -long pulses have a reduced bandwidth of approximately 10 kHz. In case of 100- μs -long excitation pulses, the Rabi frequency is such that only spins with $|\delta|/(2\pi) \leq 5 \text{ kHz}$ will contribute to the signal. This corresponds to a dispersion of only 5% for the expected Purcell relaxation times, which is negligible. To illustrate the averaging effect, two inversion-recovery curves are shown in Extended Data Fig. 1b, with readout pulses of 5 μs and 100 μs . The former yields $T_1 = 0.65 \text{ s}$, which is a factor two higher than predicted by the Purcell effect, whereas the latter yields the expected value $T_1 = 0.35 \text{ s}$.

Therefore, Fig. 2d shows an inversion-recovery sequence that has a read-out echo sequence with a narrow bandwidth ($t_\pi = 100 \mu\text{s}$, $t_{\pi/2} = t_\pi/2$) to suppress contributions from spins with a lower decay rate, and an inversion pulse with a large bandwidth ($t_\pi = 5 \mu\text{s}$) to maximize the efficiency of the inversion.

Given that the spin energy relaxation time T_1 is of the order of 1 s, we choose a repetition rate γ_{rep} that is sufficiently low to allow full relaxation of the spins between successive inversion-recovery sequences: $\gamma_{\text{rep}} = 0.04 \text{ Hz}$.

Experimental determination of spin-cavity-detuning-dependent relaxation rates. The spins are detuned from the cavity by applying an additional bias pulse on one of the Helmholtz coils used to apply the static field \mathbf{B}_0 . The extra bias pulse is output by a pulse generator with 50 Ω output impedance placed in parallel to the d.c. supply of one of the Helmholtz coils. To minimize the effect of transients due to the 1-Hz bandwidth of the coils, buffer times of 1 s are added after ramping the coil up and down. To limit the loss of signal during these buffer times, we use an angle $\theta = 45^\circ$ and work with resonator B in order to have a longer $T_1(0) = 1.68 \text{ s}$. Applying a magnetic-field pulse to a single coil instead of both coils perturbs θ by at most 4° . The value of $T_1(0)$ was measured with inversion recovery. All the data presented in Fig. 3 and in Extended Data Fig. 2 were acquired in a separate run. The quality factor of resonator B decreased from $Q = 1.07 \times 10^5$ to $Q = 8.9 \times 10^4$ owing to slightly higher losses, yielding the resonator bandwidth $\kappa/(2\pi) = 82 \text{ kHz}$.

To observe the long relaxation times, such as those measured in Fig. 3, inversion recovery is not an ideal method. When the spin linewidth is broader (about 20 times) than the excitation bandwidth and when the thermalization time is very long, one can observe polarization mixing mechanisms^{35,36}, spectral and spatial spin diffusion being the most relevant to our case, because the spin system is composed of only one species. If we try to measure the relaxation from spins that have been detuned by an amount $\delta/(2\pi) = (\omega_s - \omega_0)/(2\pi) = 3.8 \text{ MHz}$ during a lapse of time T with an inversion-recovery sequence (Extended Data Fig. 2a), then we observe a double-exponential relaxation (Extended Data Fig. 2d, green), which we attribute to the existence of a spin-diffusion mechanism.

Spin diffusion is prevented by suppressing any polarization gradient along the spin line, which leads us to use a saturation-recovery scheme instead of inversion recovery. The simplest saturation-recovery scheme (Extended Data Fig. 2b) consists of sending a strong microwave tone that results in the saturation of the line, producing an incoherent mixed state with the population evenly distributed between excited and ground states. Nevertheless, a relaxation time measured using this scheme still yields a double-exponential decay (Extended Data Fig. 2d, orange), with time constants similar to those for the inversion recovery case. This implies that the saturation of the line is insufficient.

To improve the saturation, we can sweep the magnetic field during the saturation pulse to bring different subsets of the spin line to resonance and realize a full saturation. The adopted sweep scheme is shown in Extended Data Fig. 2c. The corresponding relaxation curve fits well to a simple exponential decay (Extended Data Fig. 2d, blue), indicating the suppression of the spin-diffusion effect.

We further check the quality of the saturation by measuring the polarization across the full spin linewidth immediately after saturation. To realize such scans (Extended Data Fig. 2e), we apply the relevant saturation pulse at ω_0 , then apply a magnetic field pulse $B_\delta = (\omega_s - \omega_0)/\gamma_e$ and measure the echo signal $A_Q(\omega_s)$ with a Hahn echo sequence. When no saturation pulse is applied, the measured echo

signal $A_{Q0}(\omega_s)$ is a measure of the full polarization $-\langle S_z(\omega_s) \rangle = +1$ (Extended Data Fig. 2e, black curve) and shows the natural spin linewidth. When studying an excitation pulse, the polarization of the spins is $-\langle S_z(\omega_s) \rangle = A_Q(\omega_s)/A_{Q0}(\omega_s)$, in which $A_Q(\omega_s)$ is the measured echo signal. Therefore, $-\langle S_z(\omega_s) \rangle = -1$ indicates full inversion, $\langle S_z(\omega_s) \rangle = 0$ indicates saturation and $-\langle S_z(\omega_s) \rangle = +1$ indicates return to thermal equilibrium. The green, orange and blue curves are taken after a π pulse, after saturation without field sweep and after saturation with field sweep, respectively. At resonance, we expect a change of S_z from -1 to $+1$ for a π pulse and from -1 to 0 for a saturation pulse. Owing to the coil transient time, all three curves show a partial relaxation. If the saturation was optimal and no partial relaxation was occurring, then we should observe $S_z = 0$ for any detuning δ . For the two saturations (with and without field sweep) studied here, only that with field sweep equally saturates the line. The basic saturation with field sweep has a bandwidth of approximately 250 kHz and the bandwidth of the π pulse is similar to that of the cavity $\kappa/(2\pi) = 82$ kHz. This finding confirms that spin diffusion is fully suppressed only in a scheme of saturation with field sweep, to yield a simple exponential-decay relaxation. This scheme is used to measure the T_2 relaxation rates at different detunings δ shown in Fig. 4.

The global fit shown in Fig. 4c is obtained using $[T_1(\delta)]^{-1} = T_p + T_{NR}$, which may be expressed as $[T_1(0)]^{-1} [1 + 4(\delta/\kappa)^2]^{-1} + T_{NR}$ to involve only experimentally determined parameters. Indeed, κ is precisely determined by measuring the quality factor of the resonator at low power, and $T_1(0)$ is determined by an inversion-recovery sequence, as mentioned above. The parameter δ was determined via precise calibration of the coil pulse. Therefore, the only remaining free parameter in the fit is T_{NR} , yielding $T_{NR}^{-1} = 1,600$ s. The error bars come from the accuracy of the fits of the relaxation rates.

Practical considerations for the application of cavity-induced relaxation in magnetic resonance. The experiments described in the main text take place at low magnetic field ($B_0 < 10$ mT) and low temperature ($T \approx 20$ mK) using a dilution refrigerator. These are unusual conditions for magnetic resonance measurements; however, as we discuss below, with straightforward modifications, cavity-induced relaxation could be observed in other environments, broadening the class of spin systems that could be used.

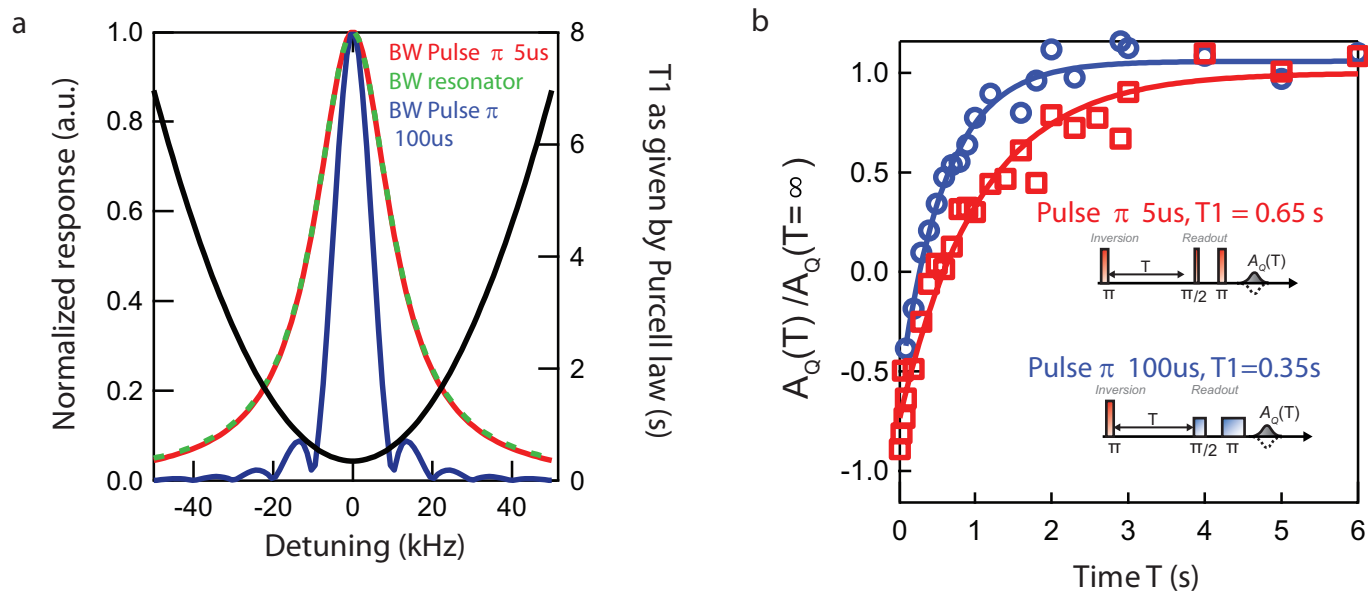
Superconducting microresonators can withstand large magnetic fields (up to approximately 1 T) while maintaining a large quality factor ($Q_i \approx 2 \times 10^5$)^{37–39} if they are patterned in metals such as Nb, NbN or NbTiN, instead of Al, as we have used. The use of these alternative metals would enable our results to be applied to a much larger class of spin systems, including typical electron spins with $g \approx 2$. Similar observations can be made for temperature: Nb, NbN and NbTiN have a higher critical temperature than does Al, which would permit the use of temperatures of 1–4 K (accessible with conventional liquid helium cryostats). However, temperature is important for reasons other than helping to maintain a small κ , because the Purcell effect brings spins into thermal equilibrium with the cavity field; for example, at the microwave frequencies used in our experiments (7.3 GHz),

temperatures below 70 mK are required for a spin polarization of $>99\%$. Higher temperatures could be used at the cost of the degree of spin polarization, but this issue could be addressed by moving to higher frequencies. A third factor when considering the operating temperature is that cavity-induced relaxation can only be exploited when it dominates over intrinsic processes such as spin-lattice relaxation. For most spin systems, this requirement translates into temperatures similar to those of liquid-helium.

The possibility of cavity-induced relaxation with conventional electron spin systems might lead to applications other than those that benefit from a faster return to thermal equilibrium to increase signal averaging rates. In particular, we consider the possibility of cavity-assisted dynamic nuclear polarization, via either the so-called solid effect or the Overhauser effect, which was recently observed in solids⁴⁰. With the solid effect, the equilibrium polarization of a nuclear spin of frequency ω_n coupled to an electron spin of frequency ω_e is enhanced by irradiating it with microwaves at $\omega_e + \omega_n$, provided the electron spins return quickly enough to equilibrium. Tuning a cavity on resonance with the electron spin transition at ω_e could provide an alternative relaxation mechanism to phonons, thereby avoiding, for example, phonon bottleneck effects and/or mitigating the need to apply large magnetic fields. With the Overhauser effect, saturating the spin transition by applying microwaves at ω_s enhances the nuclear spin polarization because of the existence of electron-nuclear spin cross-relaxation processes, which could be enhanced by tuning a cavity at $\omega_e - \omega_n$.

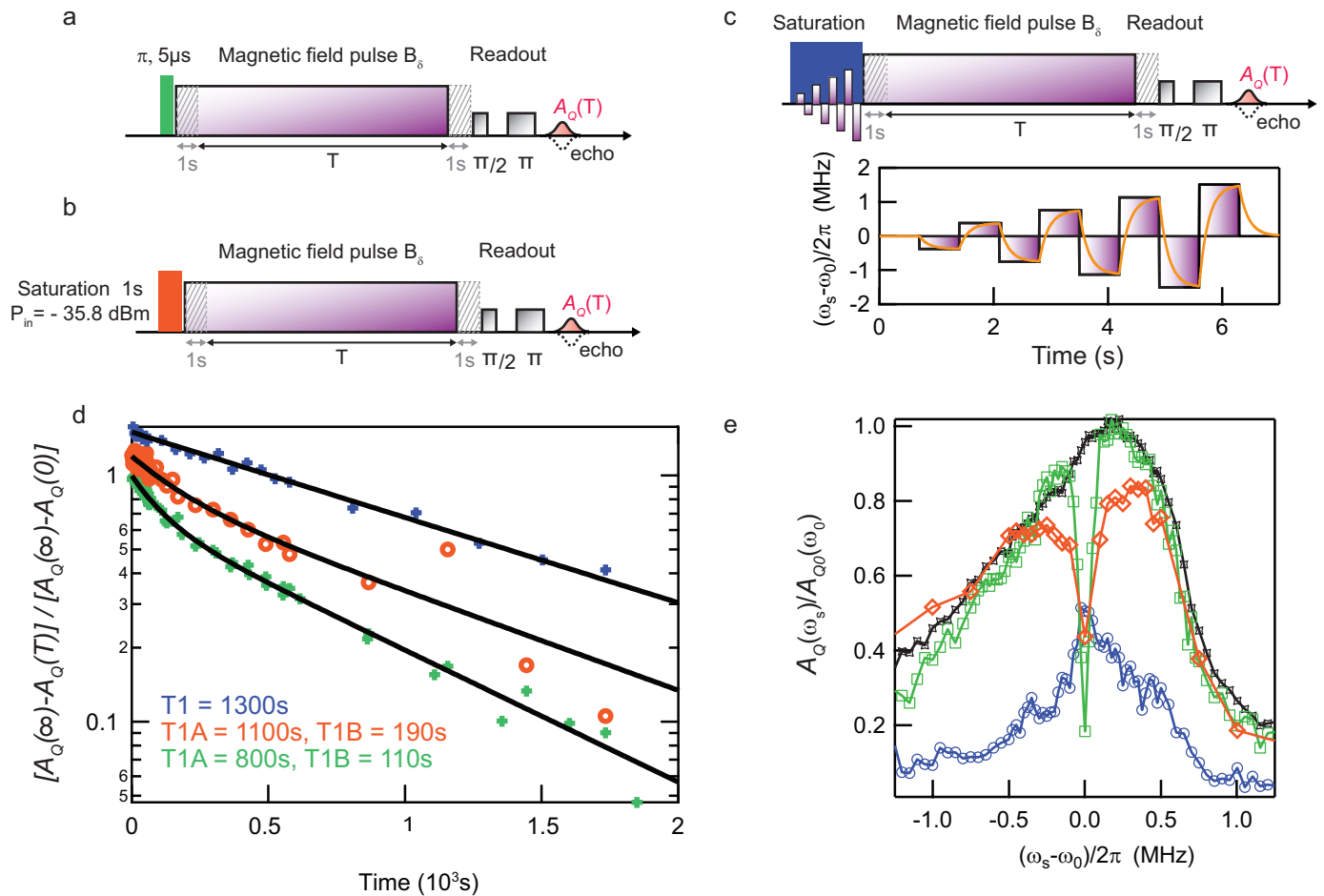
Sample size. No statistical methods were used to predetermine sample size.

31. Wolfowicz, G. *et al.* Atomic clock transitions in silicon-based spin qubits. *Nature Nanotechnol.* **8**, 561–564 (2013).
32. Van Duzer, T. & Turner, C. W. *Principles of Superconductive Devices and Circuits* 2nd edn (Prentice-Hall PTR, 1999).
33. Palacios-Lalay, A. *Superconducting Qubit in a Resonator: Test of the Leggett-Garg Inequality and Single-shot Readout*. PhD thesis, Université Pierre et Marie Curie — Paris VI (2010).
34. Mentink-Vigier, F. *et al.* Increasing sensitivity of pulse EPR experiments using echo train detection schemes. *J. Magn. Reson.* **236**, 117–125 (2013).
35. Bloembergen, N. On the interaction of nuclear spins in a crystalline lattice. *Physica* **15**, 386–426 (1949).
36. Abragam, A. *Principles of Nuclear Magnetism* Ch. IX (Oxford Univ. Press, 1983).
37. de Graaf, S. E., Davidovikj, D., Adamy, A., Kubatkin, S. E. & Danilov, A. V. Galvanically split superconducting microwave resonators for introducing internal voltage bias. *Appl. Phys. Lett.* **104**, 052601 (2014).
38. Wisby, I. *et al.* Coupling of a locally implanted rare-earth ion ensemble to a superconducting micro-resonator. *Appl. Phys. Lett.* **105**, 102601 (2014).
39. Samkharadze, N. *et al.* High kinetic inductance superconducting nanowire resonators for circuit QED in a magnetic field. Preprint at <http://arXiv.org/abs/1511.01760> (2015).
40. Can, T. V. *et al.* Overhauser effects in insulating solids. *J. Chem. Phys.* **141**, 064202 (2014).



Extended Data Figure 1 | Effect of excitation-pulse bandwidth on the measurement of T_1 . **a**, The red and blue lines shown the computed pulse bandwidth ('normalized response') for a 5- μ s π pulse and a 100- μ s π pulse, respectively, incident on a cavity with $\kappa/(2\pi) = 23$ kHz (green dashes). To illustrate the averaging effect of the pulse bandwidth on T_1 measurements, the expected Purcell T_1 curve (black line) as a function of spin-cavity detuning is plotted on the right axis, with $T_1(0) = 0.35$ s

and $\kappa/(2\pi) = 23$ kHz. **b**, T_1 measurements for two different π -pulse lengths (see insets), measured on resonance with resonator A. Spin polarization is measured with a Hahn echo sequence and A_Q is rescaled by its value for $T \gg T_1$ (' $A_Q(T = \infty)$ '). Symbols are data and solid lines are exponential fits. The 100- μ s π pulse (blue) yields $T_1 = 0.35$ s, which is in agreement with the Purcell rate. The 5- μ s π pulse (red) yields $T_1 = 0.65$ s, a factor of two greater than the accurate value.



Extended Data Figure 2 | Spectral spin diffusion. **a–c**, T_1 measurement sequence when spins are detuned from the cavity by applying a magnetic field B_δ , providing a detuning of $\delta = \omega_s - \omega_0 = 2\pi\gamma_{\text{eff}}B_\delta$, with $\gamma_{\text{eff}} = df/dB(B_0)$ the effective gyromagnetic ratio, evaluated as the derivative of $f = 2\pi\omega_s$ with respect to the applied magnetic field B at a given magnetic field B_0 . In **a**, a $5\text{-}\mu\text{s}$ π pulse is used to realize an inversion-recovery sequence; in **b**, a 1-s-long strong microwave pulse sent at cavity resonance is used to realize a saturation-recovery sequence; in **c**, a magnetic field scan (bottom panel) is used in addition to a 6-s-long strong microwave pulse to realize a saturation-recovery sequence. The expected magnetic field profile due to the coil filtering, assuming that the coil is an order-one low-pass filter with a bandwidth of 1 Hz, is shown in orange (**c**, bottom panel). **d**, T_1 measurements for sequences shown in **a** (green),

b (red) and **c** (blue) for $\delta/(2\pi) = 3.8$ MHz. The fits (black lines) to the green and red data have a double-exponential decay, whereas the fit to the blue data is a simple exponential. We attribute the double-exponential decay (with extracted characteristic times $T1A$ and $T1B$) to spin diffusion. **e**, Spectral profiles of the excitation pulse sequences shown in **a** (green), **b** (red) and **c** (blue). The sequence is as follows: send the excitation pulse, detune the spins and measure $A_Q(\omega_s)$. The black line is the reference profile without any excitation pulse, yielding the reference polarization $\langle S_z(\omega_s) \rangle = -A_{Q0}(\omega_s)/A_{Q0}(\omega_s) = -1$. When an excitation pulse is sent, we can access $\langle S_z(\omega_s) \rangle = -A_Q(\omega_s)/A_{Q0}(\omega_s)$. To conserve the line shape profile, we plotted $A_Q(\omega_s)/A_{Q0}(\omega_0)$ instead of $A_Q(\omega_s)/A_{Q0}(\omega_s)$. Neither the π profile nor the saturation profiles reach the full inversion $+1$ or the full saturation 0 at resonance; this is an artefact due to the coil transient time.

Extended Data Table 1 | Relevant Bi:Si transitions and their characteristics

Transition	df/dB	$\langle F, m_F S_x F + 1, m_F - 1 \rangle$
$ 4, -4\rangle \leftrightarrow 5, -5\rangle$	-25.1 GHz/T	0.47
$ 4, -3\rangle \leftrightarrow 5, -4\rangle$	-19.2 GHz/T	0.42
$ 4, -2\rangle \leftrightarrow 5, -3\rangle$	-13.5 GHz/T	0.37

Extended Data Table 2 | Resonator characteristics

Resonator	$\omega_r/2\pi$	Q	κ_1 (s ⁻¹)	κ_2 (s ⁻¹)	κ_L (s ⁻¹)
A	7.2467 GHz	3.2×10^5	1.3×10^4	5.8×10^4	7.5×10^4
B	7.3054 GHz	1.1×10^5	3.6×10^4	3.1×10^5	8.2×10^4